crystals

MDPI

Article

Reduced Thermal Conductivity in Ultrafast Laser Heated Silicon Measured by Time-Resolved X-ray Diffraction

Wonhyuk Jo [1,2,†], Yong Chan Cho [1,†], Seongheun Kim [3], Eric Carl Landahl [4] and Sooheyong Lee [1,5,*]

1 Korea Research Institute of Standards and Science, Daejeon 305-340, Korea; yccho@kriss.re.kr
2 Deutsches Elektronen-Synchrotron (DESY), 22607 Hamburg, Germany; wonhyuk.jo@desy.de
3 Pohang Accelerator Laboratory, Pohang 790-784, Korea; seonghkim@postech.ac.kr
4 Physics Department, DePaul University, Chicago, IL 60614, USA; elandahl@depaul.edu
5 Department of Nanoscience, University of Science and Technology (UST), Daejeon 305-340, Korea
* Correspondence: soobydoo@kriss.re.kr
† These authors contributed equally to this work.

Abstract: We investigate the effect of free carrier dynamics on heat transport in bulk crystalline Silicon following femtosecond optical excitation of varying fluences. By taking advantage of the dense 500 MHz standard fill pattern in the PLS-II storage ring, we perform high angular-resolution X-ray diffraction measurements on nanosecond-to-microsecond time-scales with femtometer spatial sensitivity. We find noticeably slowed lattice recovery at increasingly high excitation intensities. Modeling the temporal evolution of lattice displacements due to the migration of the near surface generated heat into the bulk requires reduced thermal diffusion coefficients. We attribute this pump-fluence dependent thermal transport behavior to two separate effects: first, the enhanced nonradiative recombination of free carriers, and, second, reduced size of the effective heat source in the material. These results demonstrate the capability of time-resolved X-ray scattering as an effective means to explore the connection between charge carrier dynamics and macroscopic transport properties.

Keywords: deformation potential; thermal conductivity; Silicon; time-resolved X-ray scattering; heat transport; auger recombination

Citation: Jo, W.; Cho, Y.C.; Kim, S.; Landahl, E.C.; Lee, S. Reduced Thermal Conductivity in Ultrafast Laser Heated Silicon Measured by Time-Resolved X-ray Diffraction. *Crystals* **2021**, *11*, 186. https://doi.org/10.3390/cryst11020186

Academic Editor: Sophie E. Canton
Received: 31 December 2020
Accepted: 10 February 2021
Published: 14 February 2021

1. Introduction

Bulk crystalline Silicon (Si) has attracted broad interest in commercial applications, such as transistors [1–3], photovoltaics [4], photonic-crystals [5], and sensors [6], due to its abundance, convenient manufacturing, mechanical strength, and adjustable electrical properties. In particular, a fundamental understanding of both high-speed charge carrier and thermal transport in the material provided invaluable insights for condensed matter physics and the development of next-generation technologies. However, as the decreasing size of components becomes comparable to the mean free paths of the heat carriers (electrons and phonons), the management of the heat load within such small volumes at relevant time-scales has become one of the key criteria for maintaining the functionality and reliability of these devices. Recently, it has been reported that heat flow in microscopic structures, such as thin-films or superlattices, is significantly altered from that of macroscopic materials [7,8]. In such cases, classical laws for predicting the transport mechanism, such as Fourier's law, become inadequate for describing the experimental findings. Similar difficulties may also arise under an extreme level of photoexcitation in solids, which often induces a dramatic local temperature gradients within a very short distance that may be further enhanced by nonlinear, non-radiative recombination processes. However, surprisingly little is known regarding how such non-equilibrium processes may affect the eventual outcome of macroscopic thermophysical properties, such as thermal diffusion [9]. Such scientific and practical needs combined with arrivals of femtosecond laser technologies have instigated extensive research towards understanding physical

mechanisms of heat generation (electron-phonon interactions), relaxation, and propagation at microscopic scales by using all optical pump-probe experiments [10–12]. However, past work has primarily focused on investigating electron-phonon interactions that occur at relatively early time-scales [10,13], during which the lattice system, unlike its electronic counterpart, is still out of thermal-equilibrium and, thus, thermophysical parameters are poorly-defined. Furthermore, the direct time-resolved observation of thermal transport dynamics at the bulk level remains challenging both due to the limited probe penetration depths for most optically-opaque materials as well as their inability to resolve atomic-length scale movements. A direct means to measure lattice displacement due to electron and heat propagation would remove considerable ambiguity in explaining the relevant physical phenomena. During the past decade, synchrotron based time-resolved X-ray diffraction (TRXD) has become a versatile probe for characterizing various non-equilibrium phenomena, including the transmission of heat across an interface [14], charge carrier propagation across thin-film interfaces [15] and grain boundaries [16], and the production of anisotropic strain in bulk crystal [17] and multiferroic thin film [18–20]. Additionally, laser-based table-top X-ray diffraction methods have enabled probing dynamics at ultrafast time-scales, such as unexpected anisotropic strain development from nanograin film on substrate [21] and a nanoscale transport mechanism in metallic multilayer systems [22]. More recently, X-ray free-electron laser has provided means to resolve ultrafast phase transition phenomena [23,24] that were inaccessible at storage-ring based light sources.

Here, we monitor the structural evolution of bulk Silicon crystal following femtosecond pulse-laser excitation at varying fluences by using time-resolved X-ray diffraction. Enabled by 500 MHz X-ray sampling rate and femtometer spatial sensitivity, we make quantitative measurements of changes in inter-atomic spacing due to the initial development of free carriers and heat within tens of nanoseconds as well as gradual recovery, due to the dissipation of the heat in microsecond time-scales. Our result shows the peak lattice-displacement as a function of the optical excitation intensity. A close analysis shows that the initial lattice compression, which is induced by electron deformation potential within the X-ray probe depth, monotonically increases with the laser fluence. Additionally, the expansion due to the transient temperature gradient increases and it eventually (20∼30 ns) becomes the dominant factor that drives the lattice deformation in this experiment. At much later times (>100 ns), we observe the gradual recovery of the expanded lattice toward equilibrium due to the transfer of the heat deep into the bulk. By matching the experimental data to our numerical model that is based on dynamical X-ray diffraction theory [25], we find that thermal diffusivity decreases with laser fluence. The reduction in thermal diffusivity is caused by the rapid recombination of the mobile free carriers due to the Auger effect, which ultimately constrains the distance that the free carriers are able to migrate into the bulk. In such cases, the excess energy that is imparted by the light needs to be dissipated solely via thermal diffusion that is considerably slower than charge carrier diffusion processes. Such a capability to resolve lattice deformation under extreme conditions can be readily applied to explore thermal and mechanical properties of various materials.

2. Materials and Methods

2.1. Experiment

Our experiment was performed at the 1C PAL-KRISS beamline at Pohang Light Source II (PLS-II) that is capable of generating 8.9 keV X-ray pulses with 2 ns bunch spacing and 50 ps pulse duration. The monochromatized X-ray beam with an energy bandwidth ($\Delta E/E$) of $\sim 10^{-4}$ from cryogenically-cooled double Silicon (111) crystals was cut down to 100 µm in a vertical direction and focused down to 100 µm horizontally at the sample position by a upstream toroidal mirror. Amplified Ti:Sapphire laser pulses with 800 nm central wavelength and 50 fs pulse duration operating at a repetition rate of 5 kHz is focused down to a spot size of 2 mm in diameter on the sample surface. The pump laser system is synchronized to the storage ring frequency providing timing-jitter less than 4 ps [26]. An undoped Silicon single crystal wafer (R > 1000 Ω·cm) surface-oriented to

[0 0 1] is mounted at the center of the four-circle Huber diffractometer in a vertical scattering geometry to provide an angular resolution of 0.2 millidegrees, enabling the measurement of structural deformation in a single crystal with femtometer spatial sensitivity. The diffracted X-ray photons from the sample are collected by high-speed Avalanche Photodiode (UAPD, Enertrex Corp., Crestwood, IL, USA) to resolve X-ray pulses with the 2 ns bunch spacing. Subsequently, a high bandwidth PC oscilloscope (Eon Express-CSE123G2) is used to acquire the intensity profiles of Bragg diffraction peaks from every X-ray bunch up to 3 µs (see Figure 1). We varied the absorbed pump laser fluence from 3.92 to 8.47 mJ/cm^2 at room temperature (300 K) in our experiment in order to measure the temporal evolution of X-ray diffraction peaks as a function of free-carrier density.

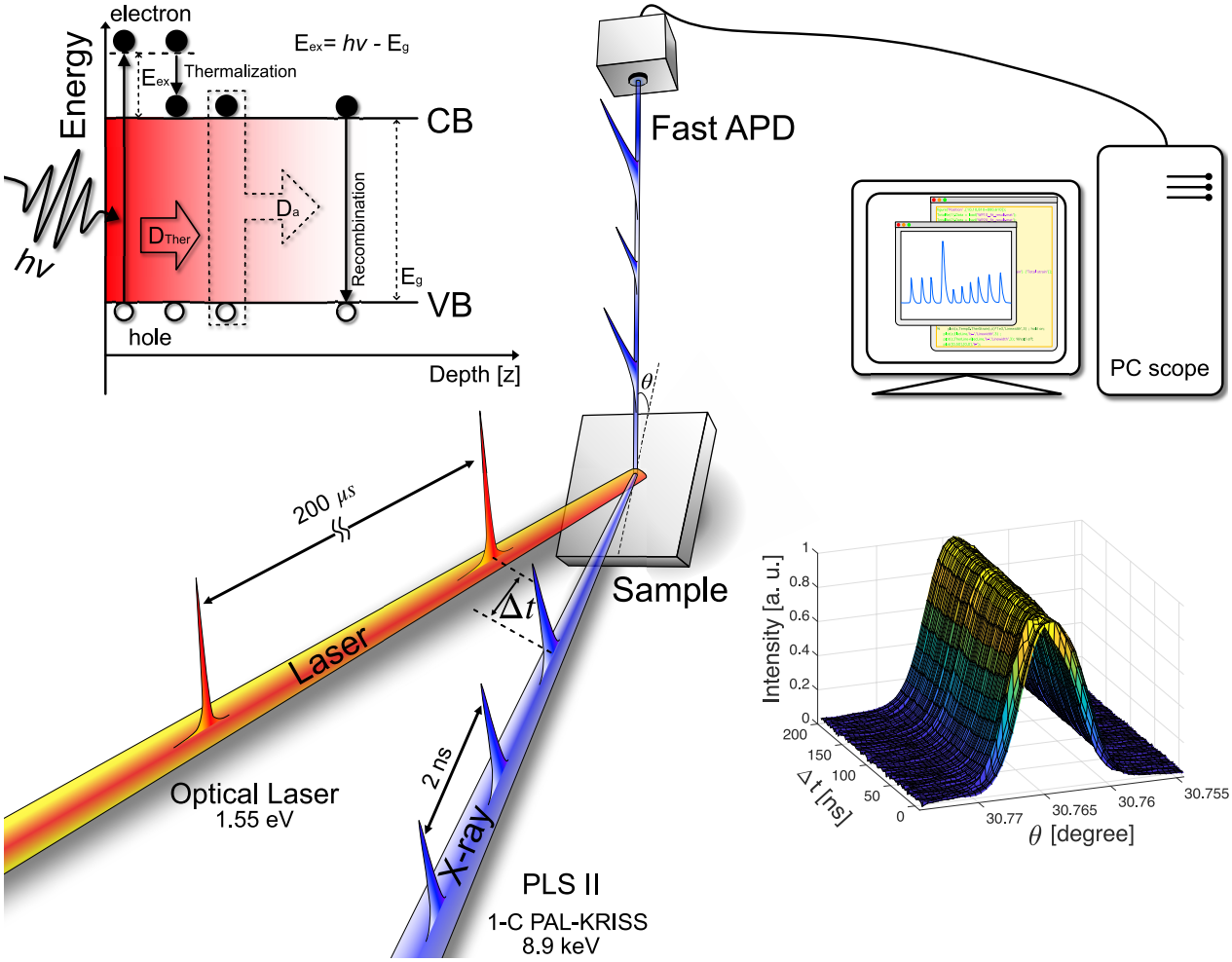

Figure 1. Schematic of time-resolved X-ray diffraction experiment at Pohang Light Source II (PLS-II). The pulse durations of X-ray and optical laser are 50 ps and 50 fs, respectively. The fast APD and on-boared digitizer allow to collect the scattered signals of each single X-ray pulses delivered with 500 MHz of electron bunch filling pattern of the storage ring. Intensity profiles of Si (0 0 4) Bragg reflections are shown in the bottom-right side. Schematic view of band structure of Si showing photo-induced dynamics in the upper-left side.

2.2. Analysis and Modeling

We measure the changes in Bragg diffraction peaks of the Si (0 0 4) reflection as a function of delay times after femtosecond laser irradiation at 2 ns intervals. A single Gaussian function was used to fit the intensity profiles of the individual rocking curves at different time-delays Δt, in which a shift of the peak center is caused by the presence of average lattice strain. In the optically excited Si, the lattice strains are mainly driven by two key sources i.e., electronic deformation potential [27] ($\eta_E(z,t)$) and thermoelastic strain

($\eta_T(z,t)$). As the optical pump beam with a photon energy greater than the electronic energy bandgap excites free carriers from the valence band, an excited carrier distribution ($\Delta n(z,t)$) is created from the surface via single and two-photon absorption processes, as follows: $\frac{dI}{dz} = -\alpha_{OPA} I(z) - \beta_{TPA} I(z)^2$, where α_{OPA}, β_{TPA}, and $I(z)$ represent single-, two-photon absorption coefficient, and absorbed intensity profile into the materials [28,29], respectively. Because the valence band electrons are involved in the atomic bonding, the $\Delta n(z,t)$ generates a strain profile with amplitude given by the deformation potential coefficient Ξ [30,31]. Within the scope of this study, it is reasonable to assume that $\Delta n(z,t)$ immediately induces the lattice stress as $\sigma_E(z,t) = \Xi \Delta n(z,t) = B_{bulk} \frac{dE_g}{dP} \Delta n(z,t)$, where B_{bulk} and $\frac{dE_g}{dP}$ denote the bulk modulus and energy gap variance with pressure, and the $\sigma_E(z,t)$ turns into $\eta_E(z,t)$ by taking into account the Young's modulus ($\eta_E(z,t) = \sigma_E(z,t)/Y_{100}$). Subsequently, the excited electrons in the conduction bands can transfer the excess energy to the cold lattice through electron-phonon (e-ph) scattering, resulting in the generation of both coherent and incoherent atomic motions [32,33]. Because such lattice thermalization processes occur much faster than the time resolution of our measurement [34], we assume that the hot electrons equilibrate with the lattice instantaneously. Accordingly, the formation of the temperature gradient into the bulk creates strain distribution, as follows: $\eta_T(z,t) = \alpha_T \Delta T(z,t)$ where α_T is a thermal expansion coefficient. The diffusion of such free charge carriers and heat within X-ray probe depth can be characterized by carefully analyzing the centroids and shapes of the diffraction peaks as a function of time.

We modeled the depth- and time-dependent free carrier and temperature distribution near the surface using coupled partial differential equations as follows [29,35,36].

$$\frac{\partial n}{\partial t} = D_a \frac{\partial^2 n}{\partial z^2} - B_{rad} n^2 - C_{Auger} n^3, \tag{1a}$$

$$\frac{\partial T}{\partial t} = D_{Ther} \frac{\partial^2 T}{\partial z^2} + C_{Auger} n^3 \frac{E_g}{C_p}, \tag{1b}$$

where D_a, D_{Ther}, C_p, C_{Auger}, and B_{rad} denote the ambipolar diffusion coefficient, thermal diffusion coefficient, specific heat, Auger recombination rate, and radiative recombination rate, respectively. We used the D_a value of 2.4 cm^2/s, which is considerably lower than the material's intrinsic value of 18 cm^2/s, due to an enhanced carrier-carrier scattering and many-body effect at highly excited carrier concentrations [37–41]. Here, we only consider one-dimensional diffusion, since we expect very steep free carrier and temperature gradients into the bulk due to the large pump beam size as compared to the X-rays on the sample surface. We note that, during the diffusion process, the free electrons transfer a considerable amount of their energy to the lattice at the expense of electron density via Auger recombination, especially at high excitation levels. In order to compare the numerical result to the experimental data, we incorporated the strain profiles into calculating the corresponding X-ray diffraction peaks of the Si (0 0 4) reflection by solving the Takagi–Taupin equations [25]. Details of the simulation procedure are elaborated elsewhere [41].

3. Results

The temporal evolution of diffraction curves from the (0 0 4) Bragg reflection for the pump laser fluence of 6.3 mJ/cm^2 is shown in Figure 2b. Upon the laser excitation, the Bragg peak initially shifts toward larger angles reaching the maximal angular deviation of $\Delta\theta$ = 0.6 millidegrees at Δt = 8 ns with its peak width broadened slightly by 1 millidegrees. These changes imply the compression of the lattice parameter and formation of an inhomogeneous strain distribution inside the crystal within the X-ray probe depth. Subsequently, we observe the development of lattice expansion that fully overtakes the compression effect by Δt = 100 ns. For a more quantitative analysis, we apply Gaussian curve fitting to the experimental data and extract transient shifts of the diffraction conditions at incremental time-delays that can be converted to atomic displacements that are based on Bragg's law, $\lambda = 2d\sin\theta$, where θ, d, and λ correspond to scattering angle, lattice parameter, and

X-ray wavelength respectively. Figure 2a show the angular shifts ($\Delta\theta = \theta - \theta_B$) of the Bragg diffraction peaks as a function of time-delays at different pump laser fluences. Sharp periodic angular shifts, of which features become progressively more noticeable at the higher laser fluence, are caused by the reflection of impulsively driven coherent phonon propagation between the front and back surfaces of the sample due to the effectively infinite impedance-mismatch at the air-to-crystal interfaces [42,43]. Assuming the longitudinal sound speed of 8350 m/s, the time interval between the echoes is consistent with the round trip time of 118 ns inside the 500 μm thick Si wafer. Contrarily, the positive angular shifts at early delay times ($\Delta t < 20$ ns) indicate the transient lattice compression that is partly caused by the deformation potential along [0 0 1] direction of the Si crystal. This compressive strain contribution lasts for approximately 10∼30 ns, depending on the laser fluence level that is used in the experiment. Beyond Δt = 30 ns, the lattice parameter proceeds to expand quickly, especially at high excitation intensities. Here, the excited charge carriers impart their excess kinetic energy to lattice via Auger recombination that leads to a rapid decrease of free carrier population and enhanced lattice dilation. Therefore, the total strain profile in the laser excited Si wafer in the relevant time-scales reflects the competition between electronically-driven contraction and thermal expansion.

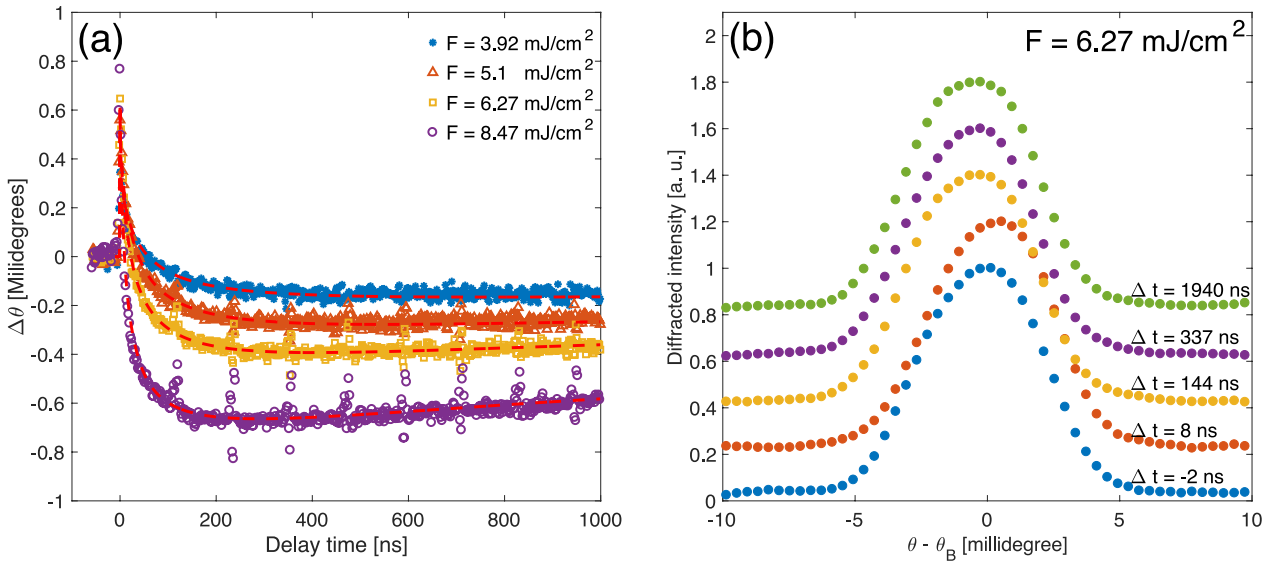

Figure 2. (**a**) Centroid shifts after the photo excitation with laser fluences. The red dashed lines represent the model-based numerical calculation result. (**b**) Temporal evolution of Si (0 0 4) X-ray rocking curves at F = 6.27 mJ/cm^2.

4. Discussion

The red dashed lines in Figure 2a show the calculated time-dependent shifts of the diffraction peaks based on our strain model and dynamical diffraction calculation that are matched to the experimental data. We note that employing the tabulated value of the thermal diffusion coefficient for bulk Si fails to reproduce the slow recovery of the strained-lattice. Therefore, the calculation was numerically matched to the data while using the material parameters that are listed in Table 1 to extract thermal diffusion coefficients for the different laser fluences. After incorporating the modified coefficient values, we find quantitative agreement between the (0 0 4) reflection and our uniaxial strain model over the entire time-scales of our measurement. Here, we neglected the strain component for the acoustic sound propagation, as it does not contribute to heating of the crystal. The result of Auger recombination rates for all pump laser fluences shows comparable values in ref. [41].

Table 1. Modeling parameters in this work.

Parameter	Used Value	Literature Value
One photon absorption coefficient (α_{OPA} [cm^{-1}])	2.25×10^3 [28]	2.25×10^3 [28]
Two photon absorption coefficient (β_{TPA} [cm/GW])	9 [28]	9 [28]
Deformation potential coefficient (Ξ [eV/Pa])	-0.9×10^{-11}	-1.2×10^{-11} [30]
Ambipolar diffusion coefficient (D_a [cm^2/s])	2.4	2.5 [40]
Radiative recombination rate (B_{rad} [cm^3/s])	1.1×10^{-14} [44]	1.1×10^{-14} [44]
Auger recombination rate (C_{Auger} [cm^6/s])	$1.33 \pm 0.3 \times 10^{-34}$	$1.33 \times 10^{-34} \sim 10^{-30}$ [41,44–46]
Thermal expansion coefficient (α_{ther} [$C^{\circ -1}$])	2.6×10^{-6} [47]	2.6×10^{-6} [47]
Specific heat (C_p [J/gC°])	0.7 [48]	0.7 [48]
Young's Modulus for [100] (Y_{100} [GPa])	130 [49]	130 [49]
Bulk Modulus (B_{bulk} [GPa])	98 [49]	98 [49]

Analysis that is based on the numerical modeling yields insights into the effect of the delicate interplay between free carriers and heat on lattice deformation. When the high pump fluence is used to excite the sample, we observe the increased thermal response and accelerated free carrier recombination. On the other hand, at relatively low excitation levels, the electronically-driven strain is more pronounced signaling longer free carrier lifetimes. In order to quantify how such transient factors affect the overall thermal diffusivity, we characterize each strain contribution. Figure 3a,b show the calculated overall strain profile as well as individual strain contributions (electronic and thermal) that result in the X-ray diffraction curve matching the experimental data at Δt = 100 ns. We expect an effectively strong Auger recombination at the highest laser fluence (F = 8.47 mJ/cm^2) based on Equation(1), which causes free carriers to recombine rapidly and transfer the excess energy that is given off by an electron to lattice [50]. Consequently, the large thermal energy is accumulated near the crystal surface until it spreads through thermal diffusion. In this case, by the time-delay of Δt = 100 ns, the thermoelastic strain is considerably greater than the deformation potential contribution due to the depleted free carrier density (See Figure 3b). Conversely, at a lower fluence of F = 3.92 mJ/cm^2, the thermal contribution is comparable to the electronic strain contribution, because the free carrier population lasts much longer, as shown in Figure 3a. Experimental confirmation is observed in the transient lattice displacement between Δt = 0 and 40 ns. The largest lattice compression is followed by rapid recovery at F = 8.47 mJ/cm^2, implying that extremely high free carrier density is both generated and then disappears within 10 ns, as shown in Figure 3c. Afterwards, thermoelastic strain predominates the lattice dynamics. On the other hand, the compression effect remains up to 40 ns for the lower excitation levels, indicating a long-lived free electron-hole pair population. Figure 4a,b show normalized electron densities that are close to the surface as a function of delay time and thermal strain distributions at Δt = 1 ns in our modeling, respectively. The higher excitation densities lead to the formation of more confined thermal distributions near the surface, since the effect of thermal diffusion is negligible at early time-scales. Consequently, the higher excitation densities result in smaller thermal distribution sizes.

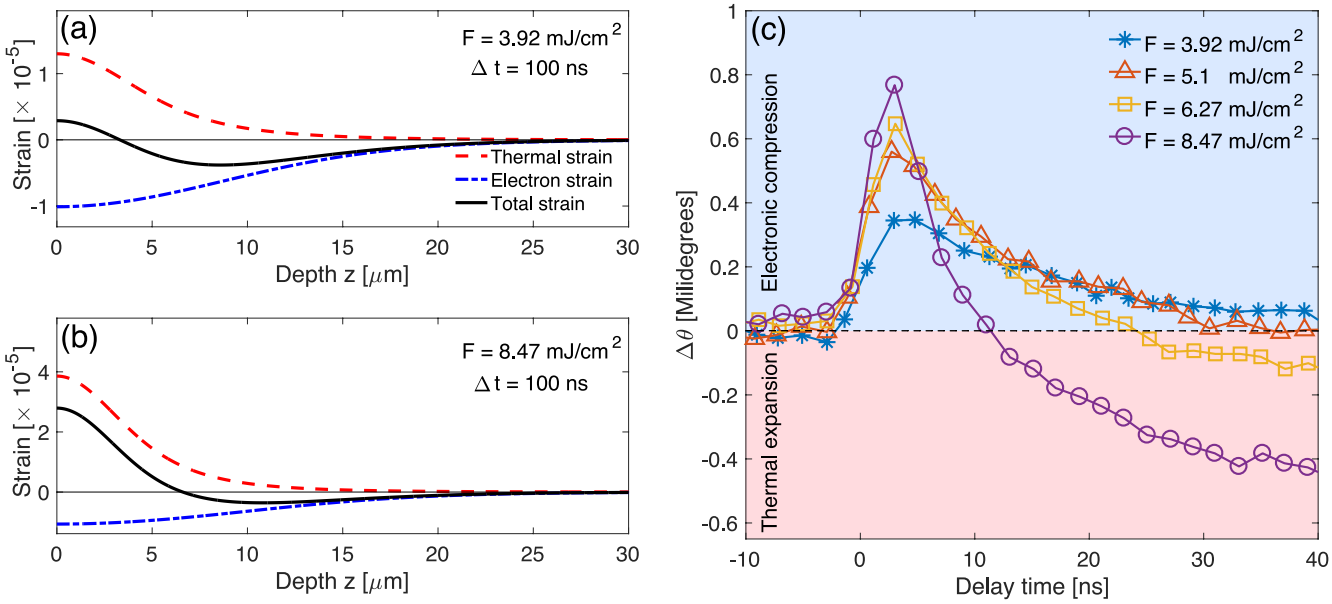

Figure 3. The distributions of the calculated thermal and electronic strains at $\Delta t = 100$ ns of $F = 3.92$ and 8.47 mJ/cm^2 in (**a**,**b**), respectively. (**c**) Centroid shifts of Bragg peaks at early delay time showing the competitions of electronic and thermal strains.

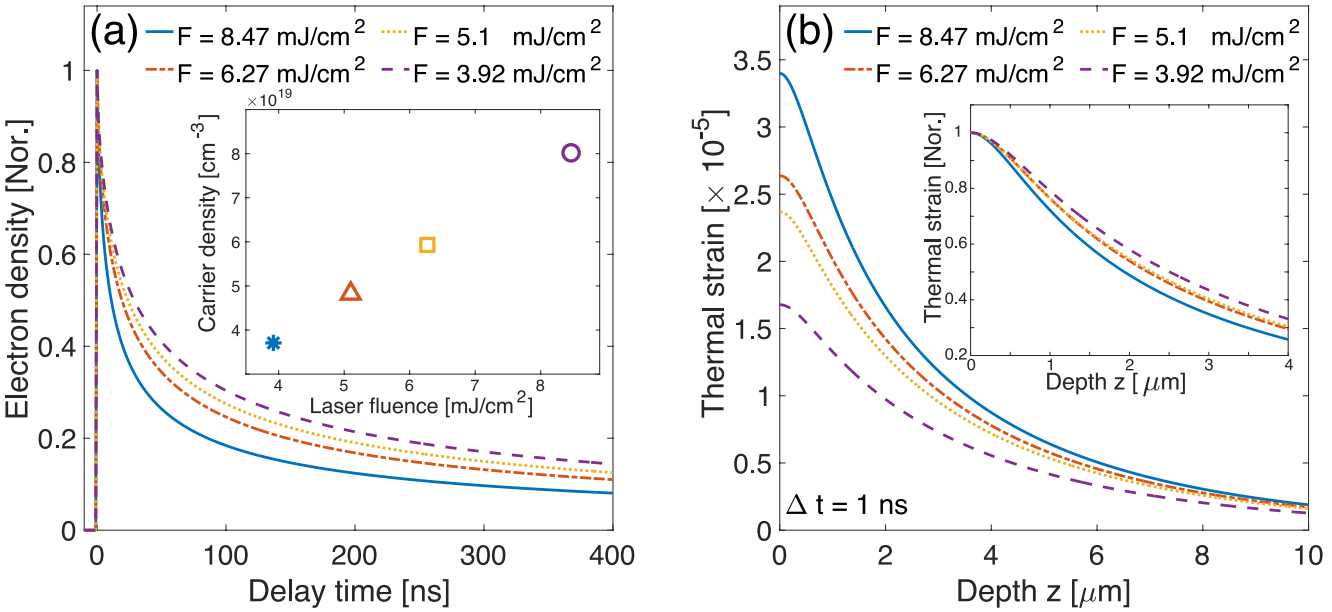

Figure 4. (**a**) Normalized electron density from the surface within 3 μm as a function of delay times, and the estimated carrier densities in the corresponding region as a function of laser fluence (inset). (**b**) Calculated distribution of thermal strains at $\Delta t = 1$ ns with laser fluence. Inset indicates that the higher laser fluence results in the smaller thermal distribution size.

We deduce the thermal conductivity k of Si for the different initial carrier concentrations by matching the numerical model to the experimental data that are based on Equation (1) and the relation $k = D_{\mathrm{Ther}}\rho C_{\mathrm{p}}$, where ρ denotes the density of the sample. We assume that the C_{p} is constant, since the estimation of temperature increment is ∼12 K at $F = 8.47$ mJ/cm^2, leading to a reduction in the k less than 4% at room temperature. Figure 5 shows the notable reduction in the thermal conductivity as compared to the bulk value k_{bulk} for increasing the carrier concentration. In particular, the values that were obtained in this work with the carrier concentration within the surface region in the range of 3.5∼8.2 $\times$ 10^{19} cm^{-3} estimated from the absorption length (10 μm) and photon energy (1.55 eV) show a consistent trend with the past work that were performed with different

techniques [9,51–53]. Nevertheless, we note that the reduced k values from 50% to 30% are noticeably smaller than that previously reported. We attribute the reduction in the thermal conductivity to two potential causes: (1) impact of e-ph scattering and (2) the role of phonon mean free path at microscopic scales. Over the past decades, the effect of e-ph scattering on heat transport was considered to be negligible at room temperature when the intrinsic phonon-phonon scattering is dominant [54,55]. However, experimental [56,57] and theoretical [58,59] studies have both recently reported that the e-ph contribution may have a significant impact on heat transport properties at high free carrier concentration in the range of 10^{19}~10^{21} cm^{-3}, even at room temperature. It has been also demonstrated that the diffusion of heat can be hindered by reduced heat source size [13]. In our case, the highly confined thermal distribution could effectively decrease the spatial extent of the heat source into the bulk, which resulted in the slower thermal transport behaviors that we observe.

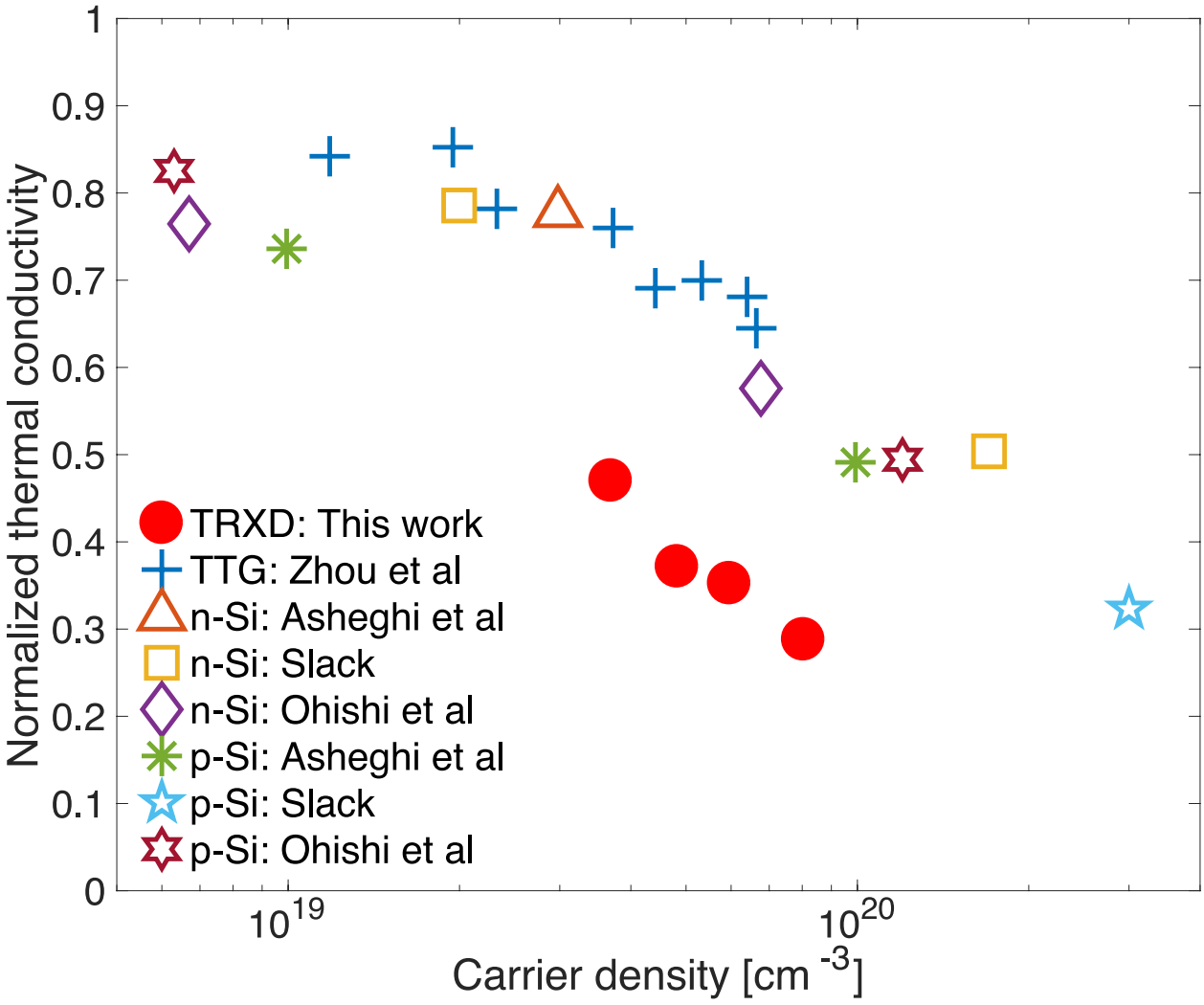

Figure 5. Measured thermal conductivity normalized to the bulk value as a function of carrier density. The carrier density in this work was estimated from mean surface carrier density within the X-ray extinction depth at $\Delta t = 0$. The results from previous research using different measurement techniques (e.g., the transient thermal grating measurement [9] and doped Si [51–53]) are also displayed.

5. Conclusions

In summary, we studied the interplay between the free carrier and thermal transport dynamics in single crystal Si upon femtosecond optical pulse excitation using high angular resolution, nanosecond time-resolved X-ray diffraction. Our experiment demonstrates that

the effective thermal conductivity of bulk Silicon depends on free carrier concentration. We attribute this behavior to the reduced free carrier lifetimes that are caused by Auger recombination, which limits the distance that the carriers diffuse into the bulk. We also find that k decreases from 50% to 30% at the carrier concentration levels in the range of $3.5 \sim 8.2 \times 10^{19}$ cm^{-3}. This reduction in thermal conductivity may be caused by electron-phonon scattering and the micro-confinement of the heat source, where the reduced spatial extent governs the phonon modes that are available to participate in the heat transfer process. Using the capability of time-resolved X-ray scattering to simultaneously measure both microscopic carrier interactions and macroscopic thermophysical properties has the potential for application to other materials, where charge carrier dynamics may significantly influence thermal transport properties, such as thermoelectrics and low dimensional systems.

Author Contributions: Conceptualization, S.L., W.J. and Y.C.C.; methodology, W.J., Y.C.C., S.K., E.C.L. and S.L.; software, W.J., S.L.; writing—original draft preparation, S.L., W.J. and Y.C.C.; writing—review and editing, all authors. All authors have read and agreed to the published version of the manuscript.

Funding: E.C.L. was supported in part by a DePaul University CSH FSRG. This research was supported by the National Research Foundation of Korea under contract No. NRF-2019K1A3A7A09033397.

Data Availability Statement: Data available on request due to restrictions e.g., privacy or ethical.

Acknowledgments: We acknowledge the support of Yongsam Kim and use of PAL-KRISS beamline at Pohang Light Source II.

Conflicts of Interest: The authors declare no conflict of interest.

References

1. Balestra, F.; Cristoloveanu, S.; Benachir, M.; Brini, J.; Elewa, T. Double-gate silicon-on-insulator transistor with volume inversion: A new device with greatly enhanced performance. *IEEE Electron Device Lett.* **1987**, *8*, 410–412. [CrossRef]
2. Walsh, S.T.; Boylan, R.L.; McDermott, C.; Paulson, A. The semiconductor silicon industry roadmap: Epochs driven by the dynamics between disruptive technologies and core competencies. *Technol. Forecast. Soc. Chang.* **2005**, *72*, 213–236. [CrossRef]
3. Khang, D.Y.; Jiang, H.; Huang, Y.; Rogers, J.A. A Stretchable Form of Single-Crystal Silicon for High-Performance Electronics on Rubber Substrates. *Science* **2006**, *311*, 208–212. [CrossRef] [PubMed]
4. Zhao, J.; Wang, A.; Green, M.A.; Ferrazza, F. 19.8% efficient "honeycomb" textured multicrystalline and 24.4% monocrystalline silicon solar cells. *Appl. Phys. Lett.* **1998**, *73*, 1991–1993. [CrossRef]
5. Notomi, M.; Shinya, A.; Mitsugi, S.; Kira, G.; Kuramochi, E.; Tanabe, T. Optical bistable switching action of Si high-Q photonic-crystal nanocavities. *Opt. Express* **2005**, *13*, 2678–2687. [CrossRef] [PubMed]
6. Agnese, R.; Ahmed, Z.; Anderson, A.J.; Arrenberg, S.; Balakishiyeva, D.; Basu Thakur, R.; Bauer, D.A.; Billard, J.; Borgland, A.; Brandt, D.; et al. Silicon Detector Dark Matter Results from the Final Exposure of CDMS II. *Phys. Rev. Lett.* **2013**, *111*, 251301. [CrossRef]
7. Siemens, M.E.; Li, Q.; Yang, R.; Nelson, K.A.; Anderson, E.H.; Murnane, M.M.; Kapteyn, H.C. Quasi-ballistic thermal transport from nanoscale interfaces observed using ultrafast coherent soft X-ray beams. *Nat. Mater.* **2010**, *9*, 26–30. [CrossRef]
8. Hu, Y.; Zeng, L.; Minnich, A.J.; Dresselhaus, M.S.; Chen, G. Spectral mapping of thermal conductivity through nanoscale ballistic transport. *Nat. Nanotechnol.* **2015**, *10*, 701–706. [CrossRef]
9. Zhou, J.; Shin, H.D.; Chen, K.; Song, B.; Duncan, R.A.; Xu, Q.; Maznev, A.A.; Nelson, K.A.; Chen, G. Direct observation of large electron–phonon interaction effect on phonon heat transport. *Nat. Commun.* **2020**, *11*, 6040. [CrossRef]
10. Koh, Y.K.; Cahill, D.G. Frequency dependence of the thermal conductivity of semiconductor alloys. *Phys. Rev. B* **2007**, *76*, 075207. [CrossRef]
11. Da Cruz, C.A.; Li, W.; Katcho, N.A.; Mingo, N. Role of phonon anharmonicity in time-domain thermoreflectance measurements. *Appl. Phys. Lett.* **2012**, *101*, 083108. [CrossRef]
12. Regner, K.T.; Sellan, D.P.; Su, Z.; Amon, C.H.; McGaughey, A.J.H.; Malen, J.A. Broadband phonon mean free path contributions to thermal conductivity measured using frequency domain thermoreflectance. *Nat. Commun.* **2013**, *4*, 1640. [CrossRef]
13. Regner, K.T.; Freedman, J.P.; Malen, J.A. Advances in Studying Phonon Mean Free Path Dependent Contributions to Thermal Conductivity. *Nanoscale Microscale Thermophys. Eng.* **2015**, *19*, 183–205. [CrossRef]
14. Sheu, Y.M.; Lee, S.H.; Wahlstrand, J.K.; Walko, D.A.; Landahl, E.C.; Arms, D.A.; Reason, M.; Goldman, R.S.; Reis, D.A. Thermal transport in a semiconductor heterostructure measured by time-resolved X-ray diffraction. *Phys. Rev. B* **2008**, *78*, 045317. [CrossRef]
15. Lee, S.; Jo, W.; DiChiara, A.; Holmes, T.; Santowski, S.; Cho, Y.; Landahl, E. Probing Electronic Strain Generation by Separated Electron-Hole Pairs Using Time-Resolved X-ray Scattering. *Appl. Sci.* **2019**, *9*, 4788. [CrossRef]

16. Jo, W.; Landahl, E.C.; DiChiara, A.D.; Walko, D.A.; Lee, S. Measuring femtometer lattice displacements driven by free carrier diffusion in a polycrystalline semiconductor using time-resolved X-ray scattering. *Appl. Phys. Lett.* **2018**, *113*, 032107. [CrossRef]
17. Lee, S.; Williams, G.J.; Campana, M.I.; Walko, D.A.; Landahl, E.C. Picosecond X-ray strain rosette reveals direct laser excitation of coherent transverse acoustic phonons. *Sci. Rep.* **2016**, *6*, 19140. [CrossRef]
18. Wen, H.; Chen, P.; Cosgriff, M.P.; Walko, D.A.; Lee, J.H.; Adamo, C.; Schaller, R.D.; Ihlefeld, J.F.; Dufresne, E.M.; Schlom, D.G.; et al. Electronic Origin of Ultrafast Photoinduced Strain in $BiFeO_3$. *Phys. Rev. Lett.* **2013**, *110*, 037601. [CrossRef] [PubMed]
19. Schick, D.; Herzog, M.; Wen, H.; Chen, P.; Adamo, C.; Gaal, P.; Schlom, D.G.; Evans, P.G.; Li, Y.; Bargheer, M. Localized Excited Charge Carriers Generate Ultrafast Inhomogeneous Strain in the Multiferroic $BiFeO_3$. *Phys. Rev. Lett.* **2014**, *112*, 097602. [CrossRef]
20. Juvé, V.; Gu, R.; Gable, S.; Maroutian, T.; Vaudel, G.; Matzen, S.; Chigarev, N.; Raetz, S.; Gusev, V.E.; Viret, M.; et al. Ultrafast light-induced shear strain probed by time-resolved X-ray diffraction: Multiferroic $BiFeO_3$ as a case study. *Phys. Rev. B* **2020**, *102*, 220303. [CrossRef]
21. Von Reppert, A.; Willig, L.; Pudell, J.E.; Rössle, M.; Leitenberger, W.; Herzog, M.; Ganss, F.; Hellwig, O.; Bargheer, M. Ultrafast laser generated strain in granular and continuous FePt thin films. *Appl. Phys. Lett.* **2018**, *113*, 123101. [CrossRef]
22. Pudell, J.; Maznev, A.A.; Herzog, M.; Kronseder, M.; Back, C.H.; Malinowski, G.; von Reppert, A.; Bargheer, M. Layer specific observation of slow thermal equilibration in ultrathin metallic nanostructures by femtosecond X-ray diffraction. *Nat. Commun.* **2018**, *9*, 3335. [CrossRef]
23. Wall, S.; Yang, S.; Vidas, L.; Chollet, M.; Glownia, J.M.; Kozina, M.; Katayama, T.; Henighan, T.; Jiang, M.; Miller, T.A.; et al. Ultrafast disordering of vanadium dimers in photoexcited VO2. *Science* **2018**, *362*, 572–576. [CrossRef] [PubMed]
24. Zalden, P.; Quirin, F.; Schumacher, M.; Siegel, J.; Wei, S.; Koc, A.; Nicoul, M.; Trigo, M.; Andreasson, P.; Enquist, H.; et al. Femtosecond X-ray diffraction reveals a liquid–liquid phase transition in phase-change materials. *Science* **2019**, *364*, 1062–1067. [CrossRef]
25. Wie, C.R.; Tombrello, T.A.; Vreeland, T. Dynamical X-ray diffraction from nonuniform crystalline films: Application to X-ray rocking curve analysis. *J. Appl. Phys.* **1986**, *59*, 3743–3746. [CrossRef]
26. Jo, W.; Lee, S.; Eom, I.; Landahl, E.C. Synchronizing femtosecond laser with X-ray synchrotron operating at arbitrarily different frequencies. *Rev. Sci. Instrum.* **2014**, *85*, 125112. [CrossRef]
27. Van de Walle, C.G. Band lineups and deformation potentials in the model-solid theory. *Phys. Rev. B* **1989**, *39*, 1871–1883. [CrossRef] [PubMed]
28. Rämer, A.; Osmani, O.; Rethfeld, B. Laser damage in silicon: Energy absorption, relaxation, and transport. *J. Appl. Phys.* **2014**, *116*, 053508. [CrossRef]
29. Williams, G.J.; Lee, S.; Walko, D.A.; Watson, M.A.; Jo, W.; Lee, D.R.; Landahl, E.C. Direct measurements of multi-photon induced nonlinear lattice dynamics in semiconductors via time-resolved X-ray scattering. *Sci. Rep.* **2016**, *6*, 39506. [CrossRef]
30. Paul, W.; Warschauer, D. Optical properties of semiconductors under hydrostatic pressure—II. Silicon. *J. Phys. Chem. Solids* **1958**, *5*, 102 – 106. [CrossRef]
31. Hu, H.; Liu, M.; Wang, Z.F.; Zhu, J.; Wu, D.; Ding, H.; Liu, Z.; Liu, F. Quantum Electronic Stress: Density-Functional-Theory Formulation and Physical Manifestation. *Phys. Rev. Lett.* **2012**, *109*, 055501. [CrossRef] [PubMed]
32. Van Driel, H.M. Kinetics of high-density plasmas generated in Si by 1.06- and 0.53-μm picosecond laser pulses. *Phys. Rev. B* **1987**, *35*, 8166–8176. [CrossRef] [PubMed]
33. Sundaram, S.K.; Mazur, E. Inducing and probing non-thermal transitions in semiconductors using femtosecond laser pulses. *Nat. Mater.* **2002**, *1*, 217–224. [CrossRef]
34. Anisimov, S.I.; Kapeliovich, B.L.; Perelman, T.L. Electron emission from metal surfaces exposed to ultrashort laser pulses. *Zhurnal Eksp. Teor. Fiz.* **1974**, *66*, 776–781.
35. Ames, W.F. Numerical Solution of Partial Differential Equations: Theory, Tools and Case Studies. *SIAM Rev.* **1986**, *28*, 92. [CrossRef]
36. DeCamp, M.F.; Reis, D.A.; Cavalieri, A.; Bucksbaum, P.H.; Clarke, R.; Merlin, R.; Dufresne, E.M.; Arms, D.A.; Lindenberg, A.M.; MacPhee, A.G.; et al. Transient Strain Driven by a Dense Electron-Hole Plasma. *Phys. Rev. Lett.* **2003**, *91*, 165502. [CrossRef]
37. Young, J.F.; van Driel, H.M. Ambipolar diffusion of high-density electrons and holes in Ge, Si, and GaAs: Many-body effects. *Phys. Rev. B* **1982**, *26*, 2147–2158. [CrossRef]
38. Rosling, M.; Bleichner, H.; Jonsson, P.; Nordlander, E. The ambipolar diffusion coefficient in silicon: Dependence on excess-carrier concentration and temperature. *J. Appl. Phys.* **1994**, *76*, 2855–2859. [CrossRef]
39. Lundstrom, M. *Fundamentals of Carrier Transport*, 2nd ed.; Cambridge University Press: Cambridge, UK, 2000.
40. Mouskeftaras, A.; Chanal, M.; Chambonneau, M.; Clady, R.; Utéza, O.; Grojo, D. Direct measurement of ambipolar diffusion in bulk silicon by ultrafast infrared imaging of laser-induced microplasmas. *Appl. Phys. Lett.* **2016**, *108*, 041107. [CrossRef]
41. Jo, W.; Landahl, E.C.; Kim, S.; Lee, D.R.; Lee, S. Delayed auger recombination in silicon measured by time-resolved X-ray scattering. *Curr. Appl. Phys.* **2018**, *18*, 1230–1234.
42. Lee, S.H.; Cavalieri, A.L.; Fritz, D.M.; Swan, M.C.; Hegde, R.S.; Reason, M.; Goldman, R.S.; Reis, D.A. Generation and Propagation of a Picosecond Acoustic Pulse at a Buried Interface: Time-Resolved X-ray Diffraction Measurements. *Phys. Rev. Lett.* **2005**, *95*, 246104. [CrossRef] [PubMed]
43. Hayashi, Y.; Tanaka, Y.; Kirimura, T.; Tsukuda, N.; Kuramoto, E.; Ishikawa, T. Acoustic Pulse Echoes Probed with Time-Resolved X-ray Triple-Crystal Diffractometry. *Phys. Rev. Lett.* **2006**, *96*, 115505. [CrossRef]
44. Schroder, D. Carrier lifetimes in silicon. *IEEE Trans. Electron Devices* **1997**, *44*, 160–170. [CrossRef]

45. Huldt, L. Band-to-band auger recombination in indirect gap semiconductors. *Phys. Status Solidi* **1971**, *8*, 173–187. [CrossRef]
46. Conradt, R.; Aengenheister, J. Minority carrier lifetime in highly doped Ge. *Solid State Commun.* **1972**, *10*, 321–323. [CrossRef]
47. Okada, Y.; Tokumaru, Y. Precise determination of lattice parameter and thermal expansion coefficient of silicon between 300 and 1500 K. *J. Appl. Phys.* **1984**, *56*, 314–320. [CrossRef]
48. Okhotin, A.S.; Pushkarskij, A.S.; Gorbachev, V.V. *Thermophysical Properties of Semiconductors*; Atomizdat: Moscow, Russia, 1972.
49. Wortman, J.J.; Evans, R.A. Young's Modulus, Shear Modulus, and Poisson's Ratio in Silicon and Germanium. *J. Appl. Phys.* **1965**, *36*, 153–156. [CrossRef]
50. Dziewior, J.; Schmid, W. Auger coefficients for highly doped and highly excited silicon. *Appl. Phys. Lett.* **1977**, *31*, 346–348. [CrossRef]
51. Slack, G.A. Thermal Conductivity of Pure and Impure Silicon, Silicon Carbide, and Diamond. *J. Appl. Phys.* **1964**, *35*, 3460–3466. [CrossRef]
52. Asheghi, M.; Kurabayashi, K.; Kasnavi, R.; Goodson, K.E. Thermal conduction in doped single-crystal silicon films. *J. Appl. Phys.* **2002**, *91*, 5079–5088. [CrossRef]
53. Ohishi, Y.; Xie, J.; Miyazaki, Y.; Aikebaier, Y.; Muta, H.; Kurosaki, K.; Yamanaka, S.; Uchida, N.; Tada, T. Thermoelectric properties of heavily boron- and phosphorus-doped silicon. *Jpn. J. Appl. Phys.* **2015**, *54*, 071301. [CrossRef]
54. Makinson, R.E.B. The thermal conductivity of metals. *Math. Proc. Camb. Philos. Soc.* **1938**, *34*, 474–497. [CrossRef]
55. Klemens, P. The Lattice Component of the Thermal Conductivity of Metals and Alloys. *Aust. J. Phys.* **1954**, *7*, 57–63. [CrossRef]
56. Yang, J.; Morelli, D.T.; Meisner, G.P.; Chen, W.; Dyck, J.S.; Uher, C. Influence of electron-phonon interaction on the lattice thermal conductivity of $Co_{1-x}Ni_xSb_3$. *Phys. Rev. B* **2002**, *65*, 094115. [CrossRef]
57. Shi, X.; Pei, Y.; Snyder, G.J.; Chen, L. Optimized thermoelectric properties of $Mo_3Sb_{7-x}Te_x$ with significant phonon scattering by electrons. *Energy Environ. Sci.* **2011**, *4*, 4086–4095. [CrossRef]
58. Liao, B.; Qiu, B.; Zhou, J.; Huberman, S.; Esfarjani, K.; Chen, G. Significant Reduction of Lattice Thermal Conductivity by the Electron-Phonon Interaction in Silicon with High Carrier Concentrations: A First-Principles Study. *Phys. Rev. Lett.* **2015**, *114*, 115901. [CrossRef] [PubMed]
59. Xu, Q.; Zhou, J.; Liu, T.H.; Chen, G. Effect of electron-phonon interaction on lattice thermal conductivity of SiGe alloys. *Appl. Phys. Lett.* **2019**, *115*, 023903. [CrossRef]